MOA-2011-BLG-293Lb: A testbed for pure survey microlensing planet detections

J.C. Yee

1. Introduction

Microlensing uses gravitational lensing of individual stars to detect planets. In a microlensing event, the light from one star, the "source", is magnified by the gravitational field of another star, the "lens". A microlensing event occurs when the paths of two stars on the sky pass very close to each other, typically less than $1''$ [An arcsecond ($''$) is 1/3600th of a degree. It may be further divided into mas=$10^{-3}''$ or μas=$10^{-6}''$.]. The magnification of the source star depends on its projected distance from the lens star, with the magnification increasing for smaller projected distances. The right-hand panel of Figure 1 shows the magnification map for a solitary lens star (a point lens), with the lens star at the center. The grayscale corresponds to the magnification of a source at that position with darker grays indicating higher magnification. Because the stars are moving, we see the brightness of the source change as a function of time because its magnification changes with its projected distance from the lens as it traces a path across this map. This "light curve" reflects the gravitational field of the lens. If there is a planet orbiting the lens star, it can create distortions in the light curve, allowing the planet to be detected. The left-hand panel of Figure 1 shows a magnification map for a planet+star lens. The difference between this map and the map for a point lens shows the effect of the planet; far from the center, the two maps are nearly identical.

The microlensing technique has been steadily finding planets for eight years. Most of these planets have been detected in "survey+followup" mode: survey groups monitor millions of stars to find microlensing events and followup groups choose which of these events to observe intensely enough to detect planets, whose perturbations to the normal

light curve typically last for only a few hours. In addition, survey groups themselves can go into followup mode when they deem an event to be of sufficient interest. Therefore, in this mode, both survey and follow-up groups may modify their target list and/or observing cadence in response to suspected planetary signals. This strategy has been effective at finding planets but makes understanding the detection efficiencies complex, although this has been done successfully for high magnification events in Gould et al. (2010a). Additionally, Sumi et al. (2010) were able to derive a slope (but not the normalization) for the mass ratio function of planets from the planetary events known at the time. Of the 13 microlensing planets published to date, only one was detected from data taken in a pure survey mode (Bennett et al. 2008).

Microlensing is entering a new era of high cadence, systematic surveys, in which survey data alone will be sufficient to detect and characterize planets with masses as small as the Earth (Gaudi 2008). Such pure-survey detections require near-24-hour monitoring with several observations of each star field per hour. Many of these future discoveries will be part of a rigorous experiment wherein the detection efficiencies are well understood because they will be found in blind or blinded (in which followup data are removed) searches, i.e. the only data used are taken with the predetermined survey frequency. Recent upgrades by the Optical Gravitational Lensing Experiment (OGLE; Chile) and Microlensing Observations in Astrophysics (MOA; New Zealand) collaborations augmented by the Wise Observatory (Israel) survey now allow near-continuous monitoring of several fields in the Galactic Bulge, 22 hours/day (Shvartzvald & Maoz 2011).

Survey-only detections, especially with the current setup, have several distinct disadvantages compared to detections that include followup data. The most prominent disadvantage that will persist for future ground-based surveys is the lack of redundancy. Having only brief overlap between data from different telescopes makes these surveys vulnerable to bad weather, which can create gaps in the data. Additionally, multiple data sets at a given epoch provide a check on systematics or other astrophysical phenomena that may create

false microlensing-like signals (see Gould et al. in prep). Simultaneous or near simultaneous observations from multiple sites are also required to measure terrestrial microlens parallax, which takes advantage of the fact that different points on the Earth have slightly different lines of sight toward the event, allowing us to measure its distance (e.g. Gould et al. 2009). Another disadvantage is that surveys are not yet able to achieve the same time frequency as followup observations, which are frequently continuous, although the current strategy for surveys is typically to switch to near continuous followup observations for events of interest. Finally, while followup groups routinely make an intensive effort to get observations at multiple wavelengths[1], survey groups are less aggressive about obtaining such observations. The trade off for these disadvantages is that surveys are able to monitor an order of magnitude more events.

Surveys face two interrelated challenges. First, there is the question of whether the survey data alone are indeed sufficient to detect planets in individual microlensing light curves in spite of the difficulties discussed above. The second challenge is to objectively define a sample of events for which the properties of the planets are well understood for the purpose of studying the ensemble of microlensing planets rather than the individuals. Gould et al. (2010a) argue that if a $\Delta\chi^2$-threshold is used to create this ensemble, it should be chosen high enough so that not only is the fit distinguishable from a point lens but also so that the great majority of planetary events can be unambiguously characterized, i.e., except for the standard microlensing degeneracies, a single solution can be identified. They estimate a threshold of $\Delta\chi^2$ =350–700 would be appropriate, but the true value is unknown. In principle, such questions could be addressed with simulations. However, in simulations it is difficult to account for real effects such as data systematics and stellar variability. Hence, using actual microlens data provides field testing that complements results from simulations.

[1]Microlensing observations are normally done in I-band (or similar filters), which is a red filter centered at ∼800nm, because that is the optical band that is most sensitive toward the Galactic Bulge. In order to derive source colors as in Sec. 3, we need observations in a different filter, for which we typically use the bluer V-band filter centered at ∼550nm.

MOA-2011-BLG-293 provides just such an opportunity for calibrating survey-only detections. The planet is robustly detected in the survey+followup data ($\Delta\chi^2 \sim 5400$), and the event was observed by all three current survey telescopes. Wise Observatory obtained data of the anomaly in their normal survey mode without changing their observing cadence, and the rest of the light curve is reasonably well covered by OGLE and MOA survey data. For this event, we are able to determine whether the survey data alone can successfully "predict" the solution determined when all of the data are included.

We begin by presenting the discovery and observations of MOA-2011-BLG-293 in Section 2. The color-magnitude diagram of the event is presented in Section 3 and used to derive the intrinsic source flux. Then, in Section 4 we present the analysis of the light curve of the event, and we compare the results with and without followup data in Section 4.2. Additional properties of the event are derived in Section 5, and the physical properties of the lens star and planet are derived from a Galactic model in Section 6. We discuss the implications of this event in Section 7.

2. Data Collection and Reduction

MOA issued an electronic alert for MOA-2011-BLG-293 [Equatorial coordinates: (RA,Dec) = (17:55:39.35, −28:28:36.65), Galactic coordinates: (l,b)=(1.52,−1.66) degrees] at UT 10:27, 4 Jul 2011 (HJD′ =HJD-2450000 = 5746.94, where HJD stands for Heliocentric Julian Date, so the units are days), based on survey observations from their 1.8m telescope with a broad R/I (a red filter with a central wavelength ∼700nm) filter and 2.2 deg^2 imager at Mt. John, New Zealand. At UT 12:45, the Microlensing Follow-Up Network (μFUN) refit the data and announced that this was a possible high-magnification event, where "high-magnification" is a peak magnification $A_{\rm max} \gtrsim 100$. At UT 17:28, μFUN upgraded to a full high-magnification alert, predicting $A_{\rm max} > 270$. They emailed subscribers to their email alert service, which includes members of μFUN and other microlensing groups, to urge observations from Africa, South America, and Israel. Additionally, a shortened version

of the alert was posted to Twitter. This prompted μFUN Weizmann to initiate the first followup observations at UT 19:45, using their 0.4m telescope (I band, a red filter centered at $\sim$800nm) at the Martin S. Kraar Observatory located on top of the accelerator tower at the Weizmann Institute of Science Campus in Rehovot, Israel. At UT 23:25, μFUN Chile initiated continuous observations using the SMARTS 1.3m telescope at CTIO. At UT 00:00 μFUN issued an anomaly alert based on the first four photometry points from CTIO, which were rapidly declining when the expected behavior was rapid brightening. The great majority of the CTIO observations were in I band, but seven observations were taken in V band (a blue filter centered at $\sim$ 650nm) to measure the source color.

MOA-2011-BLG-293 lies within the survey footprint of the MOA, OGLE, and Wise microlensing surveys and so was scheduled for "automatic observations" with high time sampling at all three observatories. MOA observed this event at least 5 times per hour. Wise observed this field 10 times during the 4.6 hours that it was visible from their 1.0m telescope, equipped with 1 deg^2 imager and I-band filter, at Mitzpe Ramon, Israel. The event lies in OGLE field 504, one of three very high cadence fields, which OGLE would normally observe about 3 times per hour. In fact, the event was observed at a much higher rate, but with the same exposure time, in response to the high-magnification alert and anomaly alert. Unfortunately, high winds prevented opening of the telescope until UT 01:02. OGLE employs the 1.3m Warsaw telescope at Las Campanas Observatory in Chile, equipped with a 1.4 deg^2 imager primarily using an I-band filter.

The data are shown in Figure 2. Several features should be noted. First, the pronounced part of the anomaly lasts just 4 hours, beginning at HJD$' = 5747.40$. The main feature is quite striking, becoming about one magnitude (see Eq. 1) brighter in about one hour. During the anomaly, the observations from Israel and those from Chile do not overlap, a point to which we return below. Finally, the CTIO data show a discontinuous change of slope ("break"), which is the hallmark of a caustic exit, when the source passes from being partially or fully inside a caustic to being fully outside the caustic (see Fig. 1). The

"caustic" is a closed curve along which the magnification of a point source would be infinite; it is highlighted in red in Figure 1. This break feature is unique to microlensing and cannot be produced by any other astrophysical phenomenon.

We construct the light curve of the event by measuring the number of photons from the target in each image from each observatory. Because each observatory has a unique setup, the number of photons it collects as a function of time, the flux scale, will be unique to that observatory. The fluxes are typically reported in magnitudes (mag) so that

$$m_1 - m_2 = -2.5 \log f_1/f_2, \tag{1}$$

where m_1 is the magnitude corresponding to the flux f_1 and m_2 is the magnitude corresponding to the flux f_2. Note that smaller magnitudes correspond to larger fluxes.

MOA and OGLE data were reduced using their standard pipelines (Bond et al. 2001; Udalski 2003) which are based on difference image analysis (DIA). In the case of the OGLE data, the source is undetected in the template image. Since the OGLE pipeline reports photometry in magnitudes, an artificial blend star with a flux of 800 units ($I_{\rm OGLE} = 20.44$) was added to the position of the event to prevent measurements of negative flux (and undefined magnitudes) at baseline when the source is unmagnified. Data from the remaining three observatories were also reduced using DIA (Wozniak 2000), with each reduction specifically adapted to that imager. Using comparison stars, the Wise and Weizmann photometry were aligned to the same flux scale as the CTIO I band by inverting the technique of Gould et al. (2010b). That is, the instrumental source color was determined from CTIO observations, and then the instrumental flux ratios (CTIO vs. Wise, or CTIO vs. Weizmann) were measured for field stars of similar color. The uncertainties in these flux alignments are 0.016 mag for Wise and 0.061 mag for Weizmann.

2.1. Data Binning and Error Normalization

Since photometry packages typically underestimate the true errors, which have a contribution from systematics, we renormalize the error bars on the data, as is done for most

microlensing events. After finding an initial model, we calculate the cumulative χ^2 distribution for each set of data sorted by magnification. We renormalize the error bars using the formula

$$\sigma_i' = k\sqrt{\sigma_i^2 + e_{\rm min}^2} \tag{2}$$

and choosing values of k and $e_{\rm min}$ such that the χ^2 per degree of freedom $\chi^2_{\rm red} = 1$ and the cumulative sum of χ^2 is approximately linear as a function of source magnification. Specifically, we sort the data points by magnification, calculate the $\Delta\chi^2$ contributed by each point, and plot $\sum_i^N \Delta\chi_i^2$ as a function of N to create the cumulative sum of χ^2, where N is the number of points with magnification less than or equal to the magnification of point N. Note that σ_i is the uncertainty in magnitudes (rather than flux). The values of k and $e_{\rm min}$ for each data set are given in Table 1. Except for OGLE, the values of $e_{\rm min}$ are all zero. This term compensates for unrealistically small uncertainties in the measured magnitude, which can happen when the event is bright and the Poisson flux errors are small.

For the MOA data, we eliminate all observations with t outside the interval $5743.5 < t({\rm HJD}') < 5749.5$ because the uncertainty in the baseline flux outside this interval is large compared to the source flux, which can bias the analysis. We also exclude all MOA points with seeing $> 5''$ because these data show a strong nonlinear trend with seeing at baseline. After making these cuts, we renormalize the data as described above.

To speed computation, the OGLE and MOA data in the wings of the event were binned. In the process of the binning, 3σ outliers were removed. This binning can increase the reduced χ^2 if the data are correlated.

3. CMD

We use the CTIO I and V band data to construct a color-magnitude diagram (CMD) of the event (Fig. 3). We measure the instrumental (uncalibrated) source color $(V-I)$ by linear regression of the V and I fluxes (which is independent of the model) and the magnitude (I) from the fitted source flux, $f_{S,{\rm CTIO}}$, of our best-fit model: $(V-I, I)_S =$

$(0.37, 22.27) \pm (0.03, 0.05)$. The position of the source relative to the field stars within $60''$ of the source (small dots) is shown in Figure 3 as the solid black dot. We calibrate these magnitudes and account for the reddening and extinction toward the field caused by intervening dust along the line of sight by assuming the source is in the Bulge of the Galaxy and calibrating the colors and magnitudes using the known intrinsic values for the red clump stars. Because of strong differential extinction across the field, we use only stars within $60''$ of the source to measure the centroid of the red clump (shown as the square with an X through it in Fig. 3). Since the event is in a low latitude field, there are more stars than is typical for bulge fields and the red-clump centroid can be reliably determined even with this restriction. In instrumental magnitudes, the centroid of the red clump is $(V - I, I)_{cl} = (0.59, 16.90)$ compared to its intrinsic value of $(V - I, I)_{cl,0} = (1.06, 14.32)$ (Bensby et al. 2011; Nataf 2012), which assumes a Galactocentric distance $R_0 = 8\,\mathrm{kpc}$ (1 kpc = 3,262 light years) and that the mean clump distance toward $l = 1.5$ lies 0.1 mag closer than R_0 (Rattenbury 2007). We can apply the offset between these two values to the source color and magnitude to obtain the calibrated, dereddened values $(V-I, I)_{S,0} = (0.84, 19.69) \pm (0.05, 0.16)$. The uncertainty in the color is derived from Bensby et al. (2011) by comparing the spectroscopic colors to the microlens colors of that sample. The uncertainty in the calibrated magnitude is the sum in quadrature of the uncertainty in $f_{S,\mathrm{CTIO}}$ from the models (0.05 mag), the uncertainty in R_0 (5%→0.1 mag), the uncertainty in the intrinsic clump magnitude (0.05 mag), and the uncertainty in centroiding the red clump (0.1 mag).

4. Analysis

4.1. Analysis of the Full Data Set

Without any modeling, we can make some basic inferences about the relevant microlens parameters from inspection of the light curve. MOA-2011-BLG-293 increases in brightness from $I \sim 19.7$ to $I \sim 15.0$, indicating a source magnification of at least 75, see Equation (1).

Additionally, except for the deviations at the peak, the event is symmetric. From these two properties, we infer that only central or resonant caustics (both of which are perturbations from a second body centered on the position of the primary) are relevant to the search for microlens models.

A point lens microlensing light curve can be described by four basic parameters: t_0, the time of closest approach, u_0, the impact parameter between the source and lens, t_E, the Einstein timescale, i.e. the time it takes the source to traverse 1 Einstein radius, and ρ, the radius of the source as a fraction of the Einstein radius. In addition, because each data set is on an arbitrary flux scale, there are two addition parameters for each data set, i, used to scale the model magnification at time t, $A(t)$, to the data flux:

$$f_{\rm mod}(t) = f_S A(t) + f_B, \tag{3}$$

where f_S is the flux of the source and f_B is the "blend" flux, the flux of all other stars blended into the point spread function. If the lens has two bodies, this introduces three additional parameters: q, the ratio of their masses, s, their projected separation in Einstein radii, and α, the angle of the source trajectory with respect to the axis connecting the two bodies. Because they are approximately constants, we use the parameters $t_{\rm eff} = u_0 t_{\rm E}$ and $t_\star = \rho t_{\rm E}$ in place of the microlens variables u_0 and ρ. We then fit models to the light curve using a Markov Chain Monte Carlo (MCMC) procedure.

Because the source has a finite size, its total magnification is found by integrating over the magnification of each point on the disk of the source. The size of the source enters the calculation as the variable ρ, but we must also take into account the limb darkening of the source, which makes the source dimmer at the edges of the disk than at the center. We adopt the "natural" linear limb-darkening coefficients $\Gamma = 2u/(3-u)$ (Albrow et al. 1999). Based on the measured position of the source in the CMD, we estimate that its temperature is $T_{\rm eff} = 5315$K and its gravity is $\log g = 4.5$ cgs. We average the linear limb-darkening coefficients for $T_{\rm eff} = 5250$K and $T_{\rm eff} = 5500$K from Claret (2000) assuming $v_{\rm turb} = 2\,{\rm km\ s^{-1}}$ to find $\Gamma_V = 0.6368$ and $\Gamma_I = 0.4602$.

The magnifications are calculated on an (s, q) grid, using the "map-making" technique (Dong et al. 2006) in the strong finite-source regime and the "hexadecapole" approximation (Pejcha & Heyrovský 2009; Gould 2008) in the intermediate regime.

We began by searching a grid of s and q to obtain a basic solution for the light curve. For central caustic crossing events like this one, there is a well known degeneracy between models with close topologies ($s < 1$) and wide topologies ($s > 1$) (Griest & Safizadeh 1998, e.g.). We initially searched a broad grid for close topologies and then used the results to inform our search for wide solutions, since to first order, $s \rightarrow s^{-1}$. The basic model from this broad grid has $s \sim 0.55$, $q \sim 0.005$, and $\alpha \sim 220^\circ$, such that the source passes over one of the points at the "back end" of a central caustic. This caustic is created by a two-body lens with a mass ratio similar to that of a massive Jovian planet orbiting a star. Figure 1 shows this basic geometry with the source trajectory relative to the caustic structure. The bump in the light curve at HJD$' \sim 5747.45$ is created when the source passes over the point of the caustic.

Because the Wise and Weizmann data only overlap with other data sets where their errors are extremely large, there is some concern that the parameters of the models will be poorly constrained, since within the standard modeling approach the flux levels of these data can be arbitrarily adjusted up or down relative to the other data (see Eq. 3). However, from the flux alignment described in Section 2, we have an estimate of $f_{S,i}$ for these data relative to $f_{S,\mathrm{CTIO}}$. This alignment gives us an independent means to test the validity of our model. If the model is correct, then the values of $f_{S,\mathrm{Wise}}$ and $f_{S,\mathrm{Weizmann}}$ should agree with $f_{S,\mathrm{CTIO}}$ within the allowed uncertainties. Alternatively, if we include the flux-alignment constraint in the MCMC fits, the solution should not change significantly.

We incorporate the flux-alignment constraint in a way that is parallel to the model constraints from the data, i.e., by introducing a χ^2 penalty:

$$\chi^2_b = \sum_i \frac{(f_{S,\mathrm{CTIO}} - f_{S,i})^2}{\sigma^2_{\mathrm{flux},i}}; \quad \sigma_{\mathrm{flux},i} = \frac{\ln 10}{2.5} \left(\frac{f_{S,\mathrm{CTIO}} + f_{S,i}}{2} \right) \sigma_i, \tag{4}$$

where i corresponds to the observatory with the constraint, and σ_i is the uncertainty in

magnitudes of the flux alignment for that observatory. In the absence of any constraints, the flux parameters for each observatory, $f_{S,i}$ and $f_{B,i}$, are linear and their values for a particular model can be found by inverting a block-diagonal covariance matrix, b. We include the flux constraints by adding half of the second derivatives of χ^2_b to the b matrix:

$$\Delta b(f_{S,i}, f_{S,k}) = \frac{2\delta_{ik} - 1}{\sigma^2_{\mathrm{flux},i}}, \tag{5}$$

where k =CTIO and δ_{ik} is a Kronecker-delta. This couples formerly independent 2×2 blocks. Strictly speaking, the equation for $\sigma_{\mathrm{flux},i}$ given in Equation (4) is a numerical approximation. Therefore, we iterate the linear fit until the value of $\sigma_{\mathrm{flux},i}$ is converged, which typically occurs in only a few iterations.

We refined the (s, q) grid around our initial close solution, fitting the data both with and without flux-alignment constraints. The mean and $1\,\sigma$ confidence intervals for the parameters from these two fits are given in Table 2. There are only small quantitative differences between the two solutions, and nothing that changes the qualitative behavior of the model. The slight increase in χ^2 is expected because of the additional term due to the flux constraints. After finding this close solution, we repeated the grid with $s \rightarrow s^{-1}$ to identify the wide solution. The parameters of this solution are also given in Table 2 both with and without flux-alignment constraints. The close solution is mildly preferred over the wide solution by $\Delta\chi^2 \sim 3$, so we quote the values for the flux-constrained close solution:

$$q = 5.3 \pm 0.2 \times 10^{-3} \qquad s = 0.548 \pm 0.005, \tag{6}$$

noting that the two topologies give very similar solutions (except $s \rightarrow s^{-1}$).

Additionally, we searched for a parallax signal in the event by adding two additional free parameters to the fit for the close solution: $\pi_{\mathrm{E},N}$ and $\pi_{\mathrm{E},E}$, the North and East components of the parallax vector (e.g., Gould 2004). The parallax effect is created by different lines of sight toward the event either due to the motion of the Earth during the event or the different locations of two observatories on the Earth's surface; this effect lets us measure the distance to the event. The parameters of this fit are given in Table 2. No parallax signal was

detected, and we found no interesting constraints on these parameters. The χ^2 improves for fits including parallax by only $\Delta\chi^2 = 7$ for two additional degrees of freedom. In some cases, even when parallax is not detected, meaningful upper limits can be placed on the parallax, but in this case we have an uninteresting 3σ constraint of $0 \leq |\pi_{\rm E}| \leq 7.8$.

4.2. Analysis with Survey-Only Data

From this analysis, we have a robustly detected planet ($\Delta\chi^2 \sim 5400$ compared to a point lens[2]) and a well-defined solution. Now we can ask whether the planet could have been detected from the survey data alone, whether the solution is well-constrained, and most importantly, whether it is the correct solution. To begin, we construct a "survey only" subset of the data. We first eliminate the Weizmann and CTIO data. Second, we "thin out" the OGLE data to mimic OGLE survey data as they would have been if there had been no high-magnification or anomaly alerts. OGLE data on several nights previous to (and following) the peak have a cadence of 1 observation per 0.015 days. We therefore adopt a subset of 18 (out of 44) OGLE points from the peak night with this sampling rate.

We repeat the analysis on this subset beginning with a broad grid search and then refining the solution following the same procedure used for analyzing the complete data set. We find that even without flux-alignment constraints, the global search isolates solutions in the general neighborhood of the solution found from the full data set. The fits to the survey-only data set are compared to fits with all data in Figure 4. Here, the $\Delta\chi^2$ of the fit compared to a point lens fit for the survey-only data is 487. This is smaller than the $\Delta\chi^2$ of any published microlensing planet. However, the parameters of the fit are well constrained

[2]Note that the numbers quoted for the point lens models include constraints from the flux alignment in the fit. Removing the flux-alignment constraints improves the χ^2, primarily because the Weizmann data can be scaled arbitrarily. However, compared to the planet fit, the point lens fit without flux-alignment constraints is still extremely poor, $\Delta\chi^2 \sim 4400$. Flux-alignment constraints have very little effect on the point lens fit to survey only data.

with errors only a factor of 1.5-2 larger compared to fits with the full data set. Applying the flux-alignment constraint to this model confirms its validity, i.e., it does not appreciably change the solution (see Table 2). In this case, it is clear that the survey data are sufficient to robustly detect and characterize the planet.

5. Physical Properties of the Event

Since finite source effects are measured in this event, we can determine the angular size of the Einstein ring, $\theta_{\rm E}$, and the lens-source relative proper motion, μ. First, we estimate the angular size of the source, $\theta_\star$, from the observed color and magnitude. We transform the $(V-I)_{S,0}$ color to $(V-K)$ using the dwarf relation from Bessell & Brett (1988). Then we use the $(V-K)$ surface brightness relations from Kervella et al. (2004) to find $\theta_\star = 0.42 \pm 0.03\,\mu$as. From this we derive the lens-source relative proper motion and angular Einstein radius,

$$\mu = \frac{\theta_\star}{t_\star} = 4.3 \pm 0.3\,{\rm mas\,yr^{-1}}; \quad \theta_{\rm E} = \mu t_{\rm E} = 0.26 \pm 0.02\,{\rm mas}. \tag{7}$$

The uncertainties in these quantities come from a variety of factors. Specifically, the uncertainties in the Galactocentric distance, R_0, and the measured intrinsic brightness of the red clump, the centroiding of the red clump from the CMD, and uncertainty in the surface brightness relations. The uncertainty contributed by the surface brightness relations is 0.02 mag, and the uncertainties from the other factors are given in Section 3. The contribution of these factors can be understood from their relationship to $\theta_\star$ (Yee et al. 2009):

$$\theta_\star = \frac{\sqrt{f_S}}{Z}, \tag{8}$$

where f_S is the source flux from the microlensing model and Z captures all other factors. Taking account of all factors mentioned above, we find $\sigma(Z)/Z = 8\%$. Since the statistical error in $f_S^{1/2}$ is only 2.3%, the error in Z completely dominates the uncertainty in θ_*. In general, the error in f_S propagates in opposite directions for $\theta_{\rm E}$ and μ (Yee et al. 2009). However, in the present case, since this error is small, the fractional error in these quantities is simply that of Z, as indicated in Equation (7).

6. Properties of the Lens

6.1. Limits on the Lens Brightness

We can use the observed brightness of the event to place constraints on the lens mass. Since the source and lens are superposed, any light from the lens should be accounted for by the blend flux, $f_{B,i}$, which sets an upper limit on the light from the lens. The unmagnified source is not seen in the OGLE data. From examination of an OGLE image at baseline with good seeing, we estimate the upper limit of the blend flux to be $I_{B,0} \geq 17.77$ based on the diffuse background light and assuming that the reddening is the same as the red clump. Assuming all of this light is due to the lens, the absolute magnitude of the lens is

$$M_{I,L} > I_{B,0} + (A_{I,S} - A_{I,L}) - 5 \log \frac{D_L}{10\,\mathrm{pc}} = 3.25 + (A_{I,S} - A_{I,L}) + 5 \log \frac{R_0}{D_L}, \qquad (9)$$

where $A_{I,S}$ and $A_{I,L}$ are the reddening toward the source and lens, respectively, and D_L is the distance to the lens. Since the lens must be in front of the source, we have $A_{I,S} \geq A_{I,L}$, i.e. there is less dust between us and the lens than between us and the more distant source. Moreover, the lens should be closer than R_0 (or at any rate, not much farther). Hence, $M_{I,L} \geq 3.25$ is a conservative lower limit. From the empirical isochrones of An et al. (2007), this absolute magnitude corresponds to an upper limit in the lens mass of $M_L \leq 1.2 M_\odot$ ($M_\odot$= mass of the Sun). We conclude from these flux-alignment constraints that either the lens is a main sequence star or, if it is more massive than our upper limit of $1.2 M_\odot$, then it must be a faint stellar remnant such as a very massive white dwarf or a neutron star.

We can use our measurement of θ_E to estimate the distance to the lens based on its mass:

$$D_L = \left(\frac{\theta_\mathrm{E}^2}{\kappa M_L} \frac{1}{\mathrm{AU}} + \frac{1}{D_S} \right)^{-1} \text{ with } \kappa \equiv \frac{4G}{c^2 \mathrm{AU}} = 8.14\,\mathrm{mas}\, M_\odot^{-1}, \qquad (10)$$

where D_S is the distance to the source. If we assume the source is at 8 kpc (i.e., about 0.1 mag behind the mean distance to the clump at this location) and $M_L = 1.2 M_\odot$, we find $D_L = 7.6\,\mathrm{kpc}$. Hence, the lens could be an F/G dwarf or stellar remnant in the Bulge, or it could be a smaller star closer to the Sun.

6.2. Bayesian Analysis

Similar to Alcock et al. (1997), we estimate the mass of the lens star and its distance using Bayesian analysis accounting for the measured microlensing parameters, the brightness constraints on the lens, and a model for the Galaxy. The mathematics are similar to what is described in Section 5 of Batista et al. (2011), although the implementation is fundamentally different because we do not have meaningful parallax information. Specifically, we perform a numerical integral instead of applying the Bayesian analysis to the results of the MCMC procedure. We begin with the rate equation for lensing events:

$$\frac{d^4\Gamma}{dD_L dM_L d^2\mu} = \nu(x,y,z)(2R_{\rm E})v_{\rm rel}f(\mu)g(M_L), \tag{11}$$

where $\nu(x,y,z)$ is the density of lenses, $R_{\rm E}$ is the physical Einstein radius, $v_{\rm rel}$ is the lens-source relative velocity, $f(\mu)$ is the weighting for the lens-source relative proper motion, and $g(M_L)$ is the mass function. The vector form of the lens-source relative proper motion is $\boldsymbol{\mu}$, which can be described by a magnitude, μ, and an angle, ϕ, such that $d^2\mu = \mu d\mu d\phi$. We transform variables (see Batista et al. 2011) to find

$$\frac{d^4\Gamma}{dD_L d\theta_{\rm E} dt_{\rm E} d\phi} = \frac{2D_L^2\mu^4\theta_{\rm E}}{\kappa\pi_{\rm rel}}\nu(x,y,z)f(\boldsymbol{\mu})g(M_L). \tag{12}$$

To find the probability distribution functions for the lens, we integrate this equation over the variables θ_E and ϕ, using a Gaussian prior for θ_E with the values given in Eq. (7) and a flat prior for ϕ. We calculate μ from $t_{\rm E}$ and $\theta_{\rm E}$ using Equation (7). We also integrate over D_S, which appears implicitly in $\pi_{\rm rel}$ and $f(\mu)$. For D_S, we include a prior for the density of sources based on our Galactic model (see below) assuming the source is in the Bulge.

Three functions remain to be defined[3]: $\nu(x,y,z)$, $f(\boldsymbol{\mu})$, and $g(M_L)$. As in Batista et al. (2011), we assume $g(M) \propto M^{-1}$. For the proper motion term, we follow Equation (19) of Batista et al. (2011):

$$f_\mu \propto \frac{1}{\sigma_{\mu,N_{\rm gal}}\sigma_{\mu,E_{\rm gal}}}\exp\left[-\frac{(\mu_{N_{\rm gal}}-\mu_{{\rm exp},N_{\rm gal}})^2}{2\sigma^2_{\mu,N_{\rm gal}}} - \frac{(\mu_{{\rm E}_{\rm gal}}-\mu_{{\rm exp},E_{\rm gal}})^2}{2\sigma^2_{\mu,E_{\rm gal}}}\right]. \tag{13}$$

[3]We will neglect constants of proportionality as they are not relevant to a likelihood analysis.

Note that the variables in f_μ are given in Galactic coordinates rather than Equatorial coordinates. The transformation between the two is simply a rotation by 60°. Still working in Galactic coordinates, the expected proper motion, $\boldsymbol{\mu}_{\rm exp}$, takes into account the typical velocity of a star in the Disk, $\mathbf{v}$, and the velocity of the Earth during the event, $\mathbf{v}_\oplus = (v_{\oplus,N_{\rm gal}}, v_{\oplus,E_{\rm gal}}) = (-0.80, 28.52)\,{\rm km\,s^{-1}}$,

$$\boldsymbol{\mu}_{\rm exp} = \frac{\mathbf{v}_L - (\mathbf{v}_\odot + \mathbf{v}_\oplus)}{D_L} - \frac{\mathbf{v}_S - (\mathbf{v}_\odot + \mathbf{v}_\oplus)}{D_S}, \tag{14}$$

where $\mathbf{v}_\odot = (7, 12)\,{\rm km\,s^{-1}} + (0, v_{\rm rot})$ and $v_{\rm rot} = 230\,{\rm km\,s^{-1}}$. For the Disk we use $\mathbf{v} = (0, v_{\rm rot} - 10\,{\rm km\,s^{-1}})$ and $\boldsymbol{\sigma} = (\sigma_{\mu,N_{\rm gal}}, \sigma_{\mu,E_{\rm gal}}) = (20, 30)\,{\rm km\,s^{-1}}$, and for the Bulge $\mathbf{v} = (0, 0)\,{\rm km\,s^{-1}}$ and $\boldsymbol{\sigma} = (\sigma_{\mu,N_{\rm gal}}, \sigma_{\mu,E_{\rm gal}}) = (100, 100)\,{\rm km\,s^{-1}}$.

For the stellar density $\nu(x, y, z)$, we use the model from Han & Gould (2003) including a bar in the Bulge. We assume the Disk has cylindrical symmetry with a hole of radius 1 kpc centered at $R_0 = 8$ kpc. We limit the Bulge to $5 < D < 10$ kpc, where D is the distance from the observer along the line of sight.

For the Bayesian analysis, we use $t_E = 21.7$ days measured from the microlensing fit to the light curve. We also have the constraint from the lens brightness that $M_L = \theta_E^2/(\kappa\pi_{\rm rel}) < 1.2 M_\odot$. This analysis implicitly assumes that the lens is a main sequence star. The lens could be a stellar remnant, although this is much less likely because of their smaller relative space density. The possibility that the lens is a stellar remnant could be tested several years from now when the source and lens have moved sufficiently far apart so as to be separately resolved, i.e., in roughly $10(\lambda/1.6\mu{\rm m})(D_{\rm tel}/10{\rm m})^{-1}$ years, where λ is the wavelength of the observations and $D_{\rm tel}$ is the diameter of the telescope used, assuming the observations are diffraction limited.

The results of the Bayesian analysis are shown in Figure 5. We find that if the lens is a main sequence star, its mass is $M_L = 0.43^{+0.27}_{-0.17}\,M_\odot$ and its distance is $D_L = 7.15 \pm 0.75\,{\rm kpc}$ (median and 68% confidence interval). Hence the planet mass is $m_p = 2.4^{+1.5}_{-0.9}\,M_{\rm Jup}$ ($M_{\rm Jup}$ = mass of Jupiter). In the close solution, the projected separation is sharply peaked at $r_\perp = sD_L\theta_{\rm E} = 1.0 \pm 0.1\,{\rm AU}$. However, the wide solution, which is not strongly disfavored, gives

an alternative $r_\perp = 3.4 \pm 0.4\,\mathrm{AU}$. If we assume $a \sim r_\perp$, the planet would have a period of ~ 1.5 (close solution) or ~ 8 (wide solution) years.

7. Discussion

The lens in MOA-2011-BLG-293 consists of a super-Jupiter orbiting a probable M dwarf. The projected separation of the planet from the star is at most a few AU, making it difficult to form *in situ* if the host is indeed an M dwarf. Core accretion theory makes a general prediction that massive Jovian planets around M dwarfs should be rare (Laughlin et al. 2004; Ida & Lin 2005). While the competing gravitational instability theory can form large planets around M dwarfs (Boss 2006), these typically form farther out, so if the planet formed by this mechanism, it would either be required to have migrated significantly or the projection effects must be severe. Adaptive Optics (AO) observations, which would allow the light from the source and lens to be detected and isolated from the light of neighboring stars, can confirm the microlensing measurement of the host mass or at least place upper limits on the host mass that would confine it to the M dwarf regime. Additionally, it should be noted that this planet joins a growing number of massive planets orbiting M dwarfs discovered by microlensing (Udalski et al. 2005; Dong et al. 2009; Batista et al. 2011) and radial velocity (see Bonfils et al. 2011 for a summary and also Johnson et al. 2011).

This event also has important implications for future survey-only microlensing planet detections. Such detections will typically have a lower time sampling than is possible with dedicated followup and may have gaps in the light curve due to adverse weather conditions. It is important to know whether we can have confidence that even with only sparse survey data, the correct microlens model can be found and the addition of more data would merely lead to a refinement of the model parameters. In Section 5.2, we demonstrated that with the survey data, even though the break in the light curve is missed because of bad weather, the same solution is recovered for MOA-2011-BLG-293, albeit at much lower significance than when all the data are included ($\Delta\chi^2 \sim 500$ compared to $\Delta\chi^2 \sim 5400$). This is somewhat

surprising since it is conceivable that the loss of this feature would allow alternative solutions to the light curve. In the absence of bad weather, the signal from the planet would have been much stronger due to additional observations, although the break would still have been less well characterized because of the lower time sampling.

Although this event clearly shows a planet is detected at $\Delta\chi^2 \sim 500$ without followup data, which is formally hugely statistically significant, it is smaller than the $\Delta\chi^2$ of any published microlensing planet. Note that it is in the middle of the range of thresholds proposed by Gould et al. (2010a) for objectively defining a sample of microlensing events. The reason this threshold is not well understood is that not all microlensing events have been analyzed for the presence of planets and the focus of the analysis to date has been on obvious microlensing signals that can be picked out by eye. New analysis pipelines are being developed in parallel with the next generation surveys, which will enable the analysis of many more events. Because real microlensing data have systematics and correlated noise, the formal $\Delta\chi^2$ may belie the actual significance of a result, e.g. one would be hard pressed to publish a "3σ detection" for $\Delta\chi^2 = 9$. Signals with small $\Delta\chi^2$ have not been systematically explored, and as such, we do not know what the true limits for detection are. Furthermore, if one wants to define a $\Delta\chi^2$ threshold for a sample of events, one probably wants most of the events meeting that threshold to be "well-characterized"[4]. Consequently, this threshold may be substantially different from the minimum required to detect individual planets.

This event points to an important ongoing role for followup data in understanding the thresholds for detecting planets and defining objective samples of planets. Events like this one, which have weak detections in the survey data but are robustly characterized with followup data, can be used to probe lower $\Delta\chi^2$ signals to inform our understanding of the significance and interpretability of small signals. The parameters of the solution found with the survey data can be compared to the parameters of the model found when

[4]We will leave the exact definition of this phrase to future investigations but suggest that it might be along the lines of constraining the mass ratio to an order of magnitude at 2σ.

including the followup data, as has been done in this paper, to see what is required to distinguish between a point lens and a 2-body lens and also what is required to consider a planet "well-characterized". By analyzing a large sample of such events, we can empirically determine appropriate $\Delta\chi^2$ thresholds, or other statistics, for both detecting planets and defining objective samples.

J.C. Yee is supported by a National Science Foundation Graduate Research Fellowship under Grant No. 2009068160. This work was performed in collaboration with the OGLE collaboration, the MOA collaboration, and the μFUN collaboration.

REFERENCES

Albrow, M. D., et al. 1999, ApJ, 522, 1022

Alcock, C. et al. 1997, ApJ, 491, 436

An, D., Terndrup, D. M., Pinsonneault, M. H., Paulson, D. B., Hanson, R. B., & Stauffer, J. R. 2007, ApJ, 655, 233

Batista, V., et al. 2011, A&A, 529, 102

Bennett, D. P., et al. 2008, ApJ, 684, 663

Bensby, T., Adén, et al. 2011, A&A, 533, A134+

Bessell, M. S. & Brett, J. M. 1988, PASP, 100, 1134

Bond, I. A., et al. 2001, MNRAS, 327, 868

Bonfils, X., et al. 2011, arXiv:1111.5019

Boss, A. P. 2006, ApJ, 643, 501

Claret, A. 2000, A&A, 363, 1081

Dong, S., DePoy, et al. 2006, ApJ, 642, 842

Dong, S., et al. 2009, ApJ, 695, 970

Gaudi, B. S. 2008, in Astronomical Society of the Pacific Conference Series, Vol. 398, Extreme Solar Systems, ed. D. Fischer, F. A. Rasio, S. E. Thorsett, & A. Wolszczan, 479

Gould, A. 2004, ApJ, 606, 319

—. 2008, ApJ, 681, 1593

Gould, A., et al. 2009, ApJ, 698, 147

Gould, A., Dong, S., Bennett, D. P., Bond, I. A., Udalski, A., & Kozlowski, S. 2010a, ApJ, 710, 1800

Gould, A., et al. 2010b, ApJ, 720, 1073

Gould, A., et al 2012, in preparation

Griest, K. & Safizadeh, N. 1998, ApJ, 500, 37

Han, C. & Gould, A. 2003, ApJ, 592, 172

Ida, S. & Lin, D. N. C. 2005, ApJ, 626, 1045

Johnson, J.A., et al., arXiv:1112.0017

Kervella, P., Thévenin, F., Di Folco, E., & Ségransan, D. 2004, A&A, 426, 297

Laughlin, G., Bodenheimer, P., & Adams, F. C. 2004, ApJ, 612, L73

Nataf, D., 2012, in preparation

Pejcha, O. & Heyrovský, D. 2009, ApJ, 690, 1772

Rattenbury, N.J. 2007, MNRAS, 378, 1064

Shvartzvald, Y. & Maoz, D. 2011, MNRAS

Sumi, T. et al. 2010, ApJ, 710, 1641

Udalski, A. 2003, Acta Astron., 53, 291

Udalski, A., et al. 2005, ApJ, 628, L109

Wozniak, P. R. 2000, Acta Astronomica, 50, 421

Yee, J. C., et al. 2009, ApJ, 703, 2082

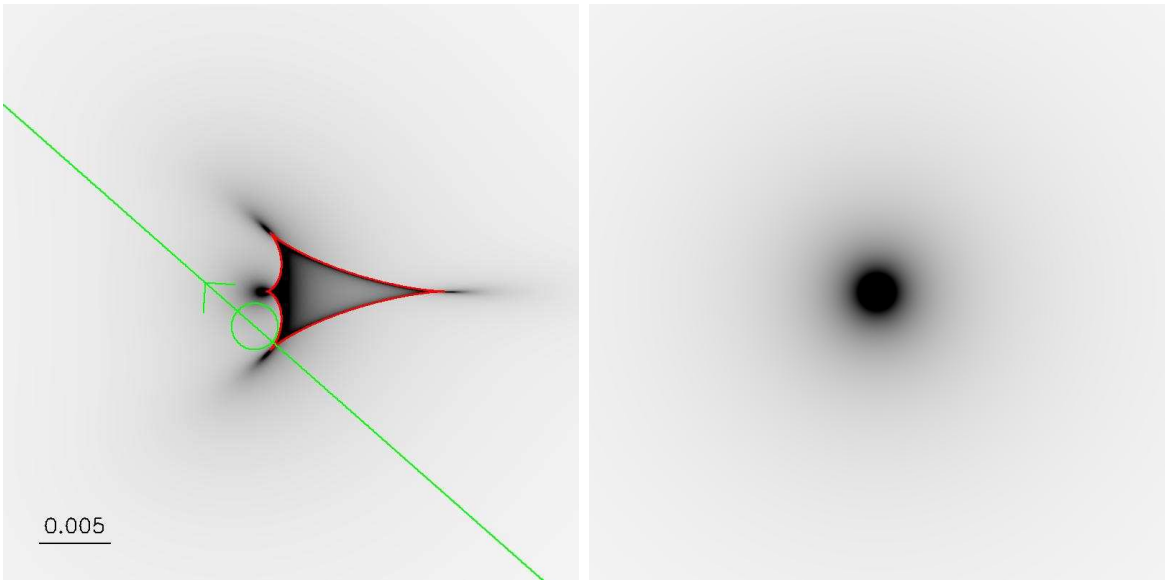

Fig. 1.— *Left panel*: Magnification map and source trajectory (*green*) of the best-fit model of MOA-2011-BLG-293. Darker gray indicates higher magnification. The circle shows the physical size of the source, and its position at the time of the caustic exit ($HJD' \sim 5747.5$). The red line traces the caustic curve where the magnification is formally infinite. The scale bar shows the scale as a fraction of the Einstein radius. The x-axis is parallel to the star-planet axis and the center of the figure corresponds to the center of magnification, close to the position of the lens star. *Right panel*: Magnification map of a point lens (no planet) for comparison.

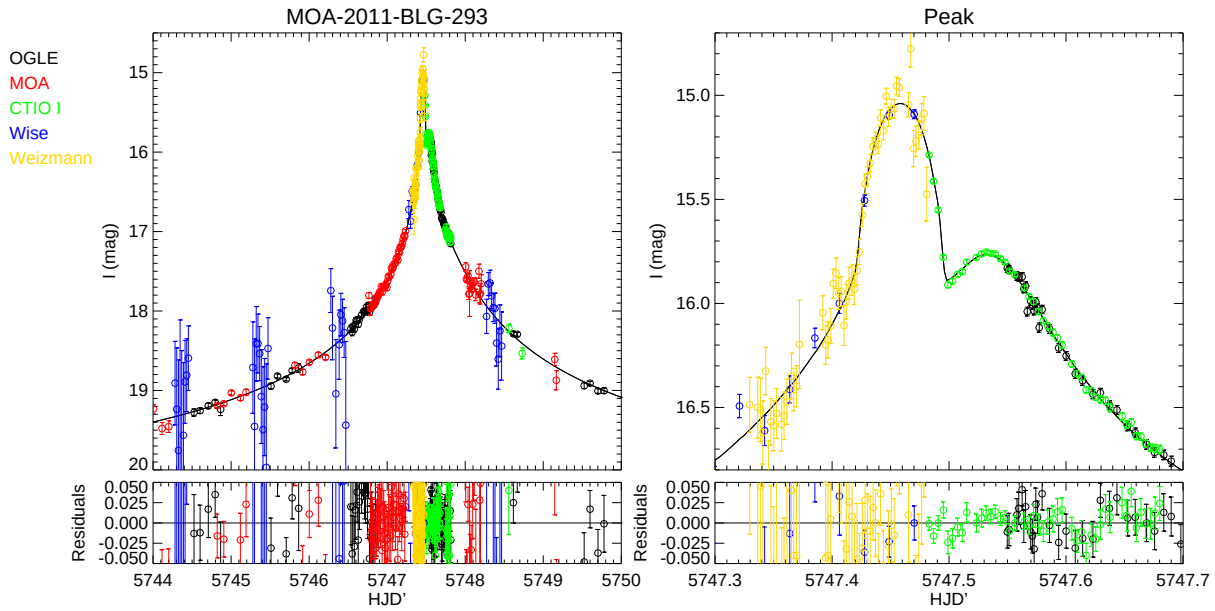

Fig. 2.— The light curve of MOA-2011-BLG-293. The left-hand panel shows a broad view of the light curve, while the right-hand panel highlights the peak of the event where the planetary perturbation occurs. The vertical axis shows brightness (increasing up), and the horizontal axis shows time in days; the times are given in HJD′=HJD−2450000 where HJD stands for Heliocentric Julian Date. Data from different observatories are represented by different colors, see legend. The black curve is the best-fit model with a close topology ($s < 1$).

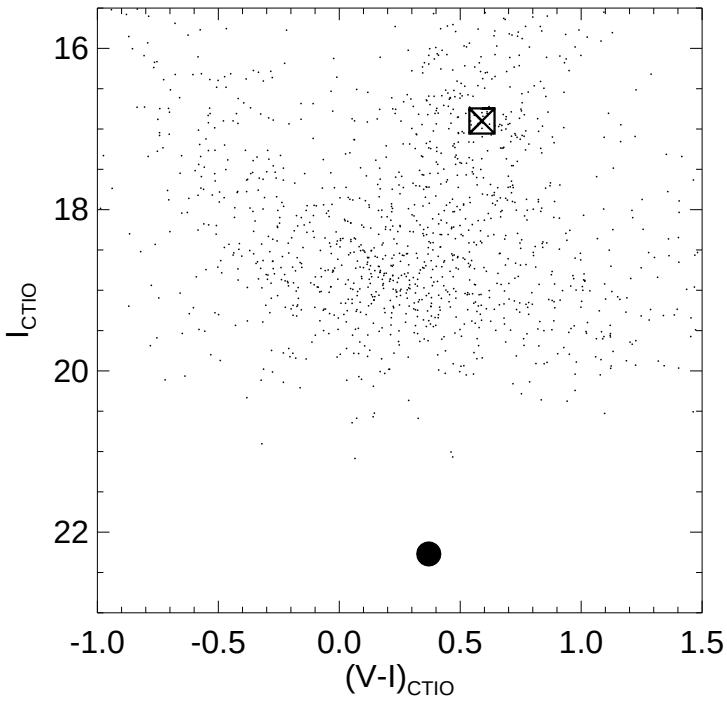

Fig. 3.— Color-Magnitude Diagram of the event in instrumental (uncalibrated) magnitudes. The horizontal axis is color, with bluer colors on the left and redder colors on the right. The vertical axis is brightness, with brighter objects at the top of the plot. The source is shown as the solid black point; the errors in the source color and magnitude are smaller than the size of the point. The centroid of the Red Clump is the open square with an X through it. The small points show the stars in the field, restricted to stars within $60''$ of the source because there is strong differential reddening on larger scales.

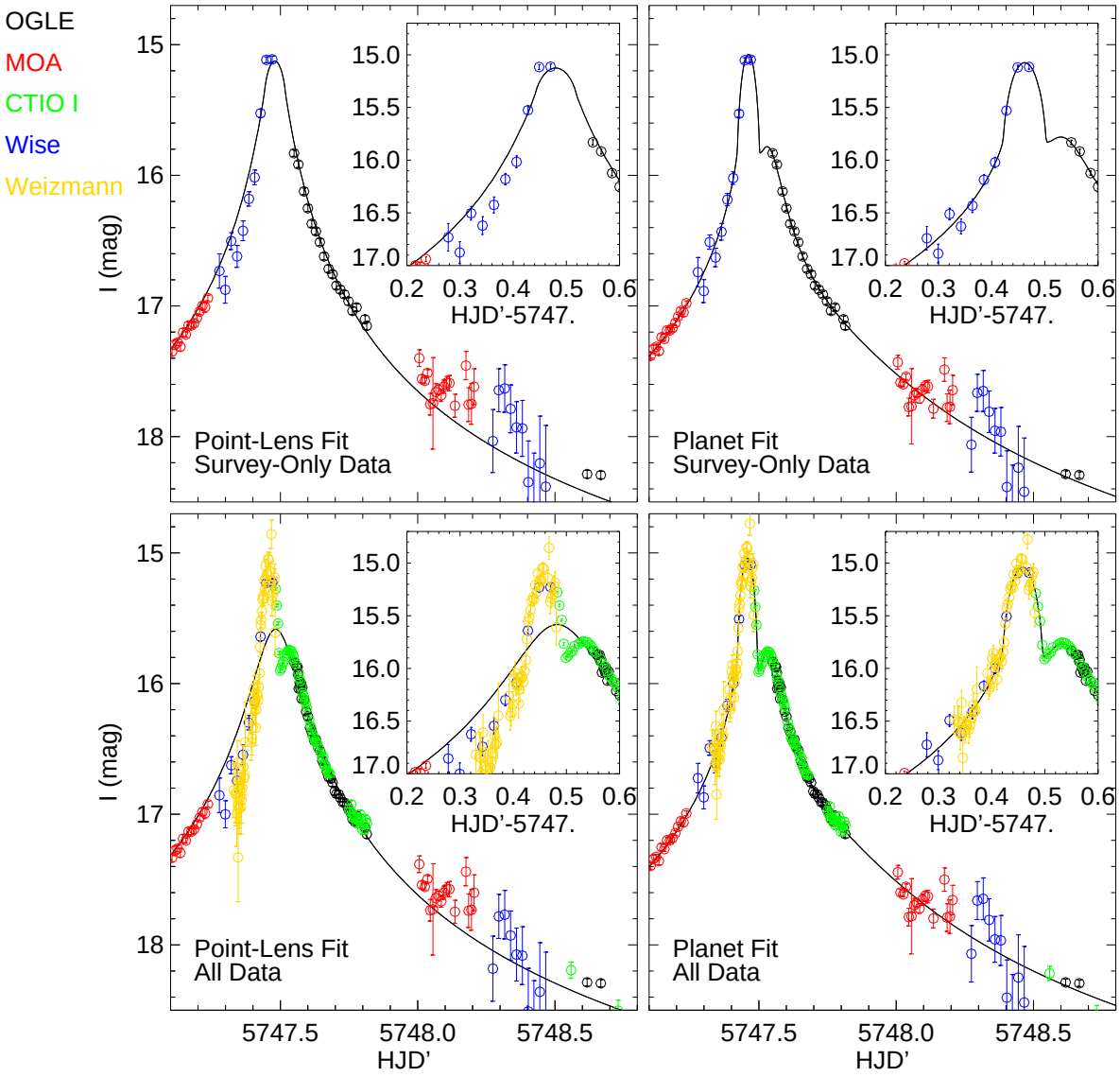

Fig. 4.— Comparison of point-lens fits (*left*) and planet fits (*right*) for "survey-only" data, (*top*) and all data (*bottom*). In both cases, the planet fit is clearly better than the point lens fit, but the difference is more significant when followup data are included. Note that for "survey-only" data the OGLE data have been thinned out to reflect the typical survey cadence.

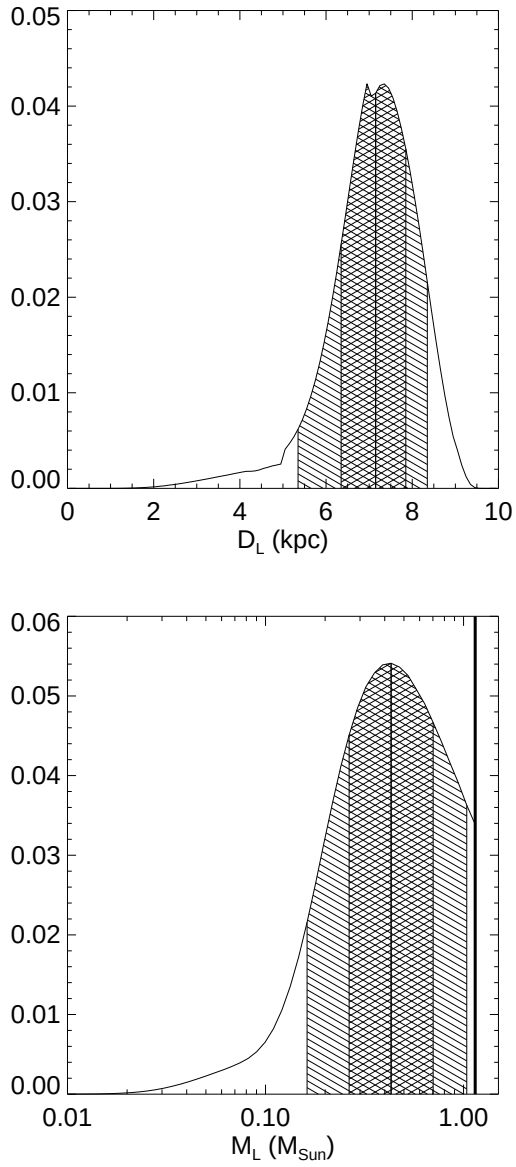

Fig. 5.— Likelihood distributions for the lens (host star) as function of its distance (*top*) and mass (*bottom*). The vertical scale is arbitrary. Masses $M_L > 1.2\,M_\odot$ are excluded by the flux-alignment constraint on the lens brightness (bold vertical line). The 68% and 90% confidence intervals about the median are indicated by the shaded regions. The discontinuities in the slope of probability distribution for the lens distance arise from overlap between the Disk and Bulge stellar density distributions. From the Galactic model priors, there is a significant probability that the host is an M-dwarf ($M_L < 0.5 M_\odot$). High-resolution imaging could confirm or contradict this by direct detection of the lens light.

Table 1. Data

Observatory	Filter	Error Renormalization Coefficients k	$e_{\rm min}$	$N_{\rm data}$
OGLE	I	1.75	0.01	274[a]
MOA	MOA-Red	1.25	0.0	78[b]
CTIO	I	1.56	0.0	63
Wise	I	1.57	0.0	49
Weizmann	I	1.74	0.0	54
CTIO[c]	V	···	···	9

[a] $N_{\rm data}$ after binning.

[b] $N_{\rm data}$ after binning. Restricted to $5743.5 < t(HJD') < 5749.5$.

[c] These data were not used in light curve modeling. They were only used to determine the color of the source.

Note. — The properties of each data set are given along with the error renormalization coefficients used to rescale the error bars (see Sec. 2.1).

Table 2. Model Parameters

Model	χ^2	$t_0 - 5747.$ (HJD′)	u_0	$t_{\rm E}$ (days)	ρ	α (°)	s	q	$\pi_{E,N}$	$\pi_{E,E}$	$\frac{f_{S,Wise}}{f_{S,CTIO}}$	$\frac{f_{S,Weizmann}}{f_{S,CTIO}}$
close	658.9377	0.4935(7)	0.0035(2)	21.67(96)	0.00164(7)	221.3(5)	0.548(6)	0.0053(2)	0.(.)	0.(.)	0.979(9)	1.09(2)
close with flux constraints	662.0860	0.4935(6)	0.0035(2)	21.75(95)	0.00163(7)	221.3(5)	0.548(5)	0.0053(2)	0.(.)	0.(.)	0.990(4)	1.08(1)
close with parallax	655.5644	0.4924(9)	0.0035(2)	21.24(95)	0.00168(8)	221.5(6)	0.552(6)	0.0054(2)	1.7(1.1)	-2.4(1.5)	0.94(2)	1.04(3)
wide	662.8497	0.4931(7)	0.0034(2)	22.49(98)	0.00158(7)	221.1(5)	1.83(2)	0.0052(2)	0.(.)	0.(.)	0.98(1)	1.08(2)
wide with flux constraints	665.9169	0.4931(6)	0.0033(1)	22.64(98)	0.00157(7)	221.1(5)	1.83(2)	0.0051(2)	0.(.)	0.(.)	0.988(5)	1.07(1)
survey only	497.3160	0.492(1)	0.0038(2)	19.8(1.0)	0.0020(2)	218(1)	0.55(1)	0.0055(4)	0.(.)	0.(.)		
survey only with flux constraints	498.8901	0.493(1)	0.0038(2)	20.0(1.0)	0.0020(2)	218(1)	0.55(2)	0.0055(4)	0.(.)	0.(.)		

Note. — The mean and root mean square errors for the parameters of each model are given along with the χ^2 for that model. The fits with "survey only" use only a subset of data representative of what would have been obtained without additional followup. Note that the parameters of these fits are very similar to the parameters of the other fits, but with slight increases in their uncertainties.